Accepted manuscript (author version)

To appear in:
International Journal of Nano Dimension (Int. J. Nano Dimens.)

Online ISSN: 2228-5059 Print ISSN: 2008-8868

Dates:
Received: 20 November 2025
Revised: 10 December 2025
Accepted: 19 December 2025

DOI: https://doi.org/10.57647/ijnd.2026.1703.07

Label-free Sensing of Thiamine, Pantothenic Acid and Pyridoxine Hydrosoluble Vitamins Using a Symmetric Photonic Heterostructure Resonator

Hadi Rahimi*

Department of Physics, Tab.C., Islamic Azad University, Tabriz, Iran

Corresponding Author: *Hadi Rahimi, h_rahimi@iau.ac.ir*

Abstract

This study presents a label-free biosensor based on a symmetric one-dimensional photonic heterostructure resonator for the refractometric detection of three water-soluble B-complex vitamins. By filling the defect cavity with vitamin solutions, the sensor generated distinct resonance shifts proportional to refractive-index changes, enabling precise molecular discrimination. Optimal performance was achieved at a 60° incidence angle under transverse-electric polarization, yielding ultra-high sensitivity (nearly 280 nm/RIU), a sharp resonance quality factor exceeding 2000, and a detection limit as low as 1.21×10^{-3} RIU, accompanied by a figure of merit greater than 800 surpassing conventional 1D photonic crystal biosensors. A strong polarization-dependent response was observed, with transverse-magnetic (TM) mode performance degrading at high angles due to Brewster's effect, confirming TE polarization as the superior sensing configuration.

Keywords: *Hydrosoluble Vitamins; Label-Free Detection; Photonic Crystals; Refractometric Sensing; Resonators.*

1. Introduction

Photonic crystals and plasmonic structures enable precise nanoscale light manipulation, allowing for the highly sensitive detection of biological and chemical substances. Recent advances have introduced platforms that strongly confine and precisely tune light. For example, combining a metal film with a photonic crystal has boosted certain optical signals by nearly a thousandfold [1]. Optical Tamm states at material interfaces can also create intense light concentration, which is highly valuable for sensing applications [2]. Other innovations include metasurfaces designed to perfectly absorb specific infrared

light, matching human absorption for potential sensing uses [3]. Platforms that enhance molecular fingerprint signals have also been developed, allowing flexible spectral tuning [4]. Furthermore, new metasurfaces with independently tunable resonances across infrared wavelengths enable sensitive biosensing and real-time monitoring of proteins, offering a powerful tool for integrated medical devices [5]. At the same time, photonic crystal fiber (PCF) sensors combined with surface plasmon resonance (SPR) are becoming powerful tools. A Kagome-lattice PCF-SPR sensor has shown excellent performance for detecting blood components [6], and reviews such as Ramola et al. [7] explain how different PCF-SPR designs can sense glucose, DNA, proteins, and even cancer cells. With the help of artificial intelligence, these sensors can be optimized for faster and more accurate detection [8, 9]. Together with other environmental sensing methods [10], these technologies are shaping a new generation of highly sensitive tools for medicine, food safety, and environmental monitoring. For non-invasive health monitoring, two dual-polarized sensors have been developed: a triple-layered sensor designed for glucose monitoring in urine to prevent diabetes [11], and a comparable "PregBiosensor" for early pregnancy detection via urine analysis to lower miscarriage risk [12].

With these developments in photonic and plasmonic technologies, researchers are now extending such sensitive detection methods to water-soluble vitamins, which require precise and label-free analysis. Many new methods use plasmonic structures such as Metal-Insulator-Metal (MIM) waveguides; for example, Shangbo et al. [13] used Fano resonance for highly sensitive vitamin detection, while Sun et al. [14] designed an S-shaped plasmonic waveguide. At terahertz frequencies, Wang et al. [15] developed a metasurface sensor that can detect vitamins C and B9 with very high accuracy, and electrochemical sensors improved with nanomaterials are widely used for vitamins like B6 [16,17]. In addition, recent studies on various nanomaterials show how tuning their optical and chemical properties can further improve detection. Examples include band-gap-tuned Ni–Co sulfide nanoparticles [18], optimized DNA-assisted CNT dispersions [19], and nanocomposites with enhanced photocatalytic

activity [20]. Other works such as Ag–Cu alloy nanoparticles that reduce bacterial activity [21] and new pyrazole derivatives with selective antibacterial effects [22] also highlight how engineered nanoscale materials can support more effective biochemical analysis.

Photonic sensing has grown rapidly, but the detection of water-soluble vitamins using photonic crystal resonators is still limited. To help fill this gap, we designed a symmetric photonic heterostructure for label-free detection of three B-complex vitamins: thiamine (B_1), pantothenic acid (B_5), and pyridoxine (B_6). The symmetric structure creates sharp resonances and strong confinement. When vitamin solutions are placed in the cavity, even small changes in refractive index lead to clear shifts in the resonance peak. The sensor works best for TE polarization at incident angle $\theta = 60^{\circ}$, offering high sensitivity, a large quality factor, and a very low detection limit. It also shows a strong figure of merit and confirms that TM polarization weakens at higher angles due to Brewster's effect, making the TE mode the preferred choice for sensing.

2. Materials and Methods

In this work, a one-dimensional (1D) symmetric heterostructure biosensor a defect layer of water-soluble vitamin solution is considered as an optical microcavity for refractometric sensing. The structure is designed as $(AB)^N /D/ (BA)^N$, where A=TiO_2 and B=SiO_2, with a defect (D) and N period. The 1D photonic crystal biosensor is superior to 2D/3D counterparts due to three key advantages: simpler optical analysis using straightforward methods like transfer matrix method versus complex finite element method simulations; easier and cheaper fabrication via standard deposition techniques compared to advanced and costly methods like electron beam lithography.

The proposed sensor model can significantly simplify the vitamin analysis process compared to conventional methods like high-performance liquid chromatography (HPLC) or enzyme-linked immunosorbent assay (ELISA). It eliminates the need for time-consuming and costly labeling steps such

as fluorescent tagging, enzyme-antibody conjugation, or chemical derivatization. Also, the sample typically requires only simple dilution, whereas methods like HPLC demand extensive extraction and purification.

The refractive index of SiO_2 and TiO_2 layers were calculated by using the Sellmeier equation. The wavelength-dependent permittivity coefficients of SiO_2 and TiO_2 are assumed as follows [23, 24]

$$\varepsilon_A = 5.913 + \frac{0.2441}{(\lambda^2 - 0.0803)},$$

$$\varepsilon_B = 1 + \frac{0.6961663\,\lambda^2}{(\lambda^2 - (0.0684043 \times 10^{-6})^2)} + \frac{0.4079426\,\lambda^2}{(\lambda^2 - (0.1162414 \times 10^{-6})^2)} + \frac{0.8974794\,\lambda^2}{(\lambda^2 - (9.806161 \times 10^{-6})^2)}. \quad (1)$$

It should be noted that all supposed materials are non-magnetic. The performance of a biosensor is mainly determined by their quality factor as

$$Q=\lambda_0/\Delta\lambda_{FWHM} \quad (2)$$

Where λ_0 is the resonant wavelength and $\Delta\lambda_{FWHM}$ represents the spectral width of the resonance peak at half maximum. Another biosensor parameter is sensitivity (S) which can be considered as

$$S = \Delta\lambda/\Delta n \quad (3)$$

Where $\Delta\lambda$ denotes the resonant wavelength shift and Δn represents the corresponding refractive index change. This relation demonstrates that the sensor's detection capability is directly proportional to the spectral displacement per refractive index variation. The third parameter is the detection limit (DL)

$$DL=\Delta\lambda_{min}/S=(\lambda_0/S.Q) \quad (4)$$

Where λ_0 is the resonant wavelength, S is the sensitivity, Q is the quality factor and $\Delta\lambda_{min}$ is the minimum detectable wavelength shift. The expression links the sensor's fundamental optical characteristics (Q, S) with its practical detection capability. Finally, the forth parameter is the figure of merit (FOM)

$$FOM = S \cdot Q / \lambda_0 \quad (5)$$

The FOM comprehensively evaluates sensor performance by combining both S and Q [25].

The optical response of the proposed structure was numerically analyzed using the transfer matrix method (TMM). The TMM is an analytical, layer-based approach. Unlike FDTD or COMSOL-type numerical solvers, The TMM does not require any spatial meshing, nodes, cells, or meshing-resolution parameters. In this method, each layer of structure is represented by a characteristic 2×2 transfer matrix that relates the forward- and backward-propagating electric fields at the input and output interfaces. The total transfer matrix of the entire stack is obtained by multiplying the individual matrices of all layers in sequence. The electric field in two adjacent layers is expressed as:

$$\begin{cases} E_1(z,\omega) = A_1 e^{ik_1 z} + B_1 e^{-ik_1 z} & ; \quad 0 < z \le d_1 \\ E_2(z,\omega) = A_2 e^{ik_2 (z-d_1)} + B_2 e^{-ik_2 (z-d_1)} & ; \quad d_1 < z \le d_2 \end{cases} \quad (6)$$

In these relations, k_1 and k_2 represent the wave numbers in the two layers .The coefficients A_1, B_1, A_2 and B_2 are determined by enforcing the boundary conditions at the interface between layers. After performing the necessary mathematical calculations, the transfer matrix is given by [26]:

$$M_j(\Delta z,\omega) = \begin{pmatrix} \cos(k_z^j \Delta z) & j/q_j \sin(k_z^j \Delta z) \\ jq_j \sin(k_z^j \Delta z & \cos(k_z^j \Delta z) \end{pmatrix} \quad (7)$$

Where $k_z^j = (\omega/c)\sqrt{\varepsilon_j}\sqrt{\mu_j}\sqrt{1-\sin^2/\varepsilon_j\mu_j}$ is the component of the wave vector along the z axis, c indicates the speed of light, $q_j = \sqrt{\varepsilon_j}/\sqrt{\mu_j}\sqrt{1-\sin^2/\varepsilon_j\mu_j}$ for TE mode. The transmission coefficient is

$$t(\omega,\theta) = \frac{2\cos\theta}{(m_{11}+m_{22})\cos\theta + i(m_{12}\cos^2\theta - m_{21})} \quad (8)$$

3. Results and Discussion

Here, a 1D heterostructure was designed as $(AB)^N$ /D/ $(BA)^N$. The structure consists of alternating layers of titanium dioxide (A=TiO_2, n_A=2.5) and silicon dioxide (B=SiO_2, n_B=1.46), arranged according to the quarter-wave thickness rule ($d=\lambda_0/4n$) at the design wavelength λ_0=800 nm. It should be noticed that because both sides of the defect layer are the same, the wave stays trapped more effectively. The corresponding physical thicknesses are d_A=80 nm and d_B=137 nm. The periodic number was set to N=7 on each side of the structure. At the center of the structure, a defect layer (D) is introduced, filled with a water-soluble vitamin solution. To ensure strong resonance within the photonic bandgap, the defect thickness is set to half-wave optical thickness, calculated as $d_D=\lambda_0/(2n_{defct})$, where $n_D=n_{defct}$ is the refractive index of the vitamin solution (see Table 1). The defect thickness was chosen approximately 300 nm for λ_0=800 nm and n_D=1.33.

Table 1: Selected water soluble vitamins with concentration of 1g/50 mL.

Vitamin	Refractive index	Reference
Vitamin B_5 (pantothenic acid)	1.3360	[18]
Vitamin B_1 (Thiamine)	1.3366	[18]
Vitamin B_6 (Pyridoxine)	1.3371	[18]

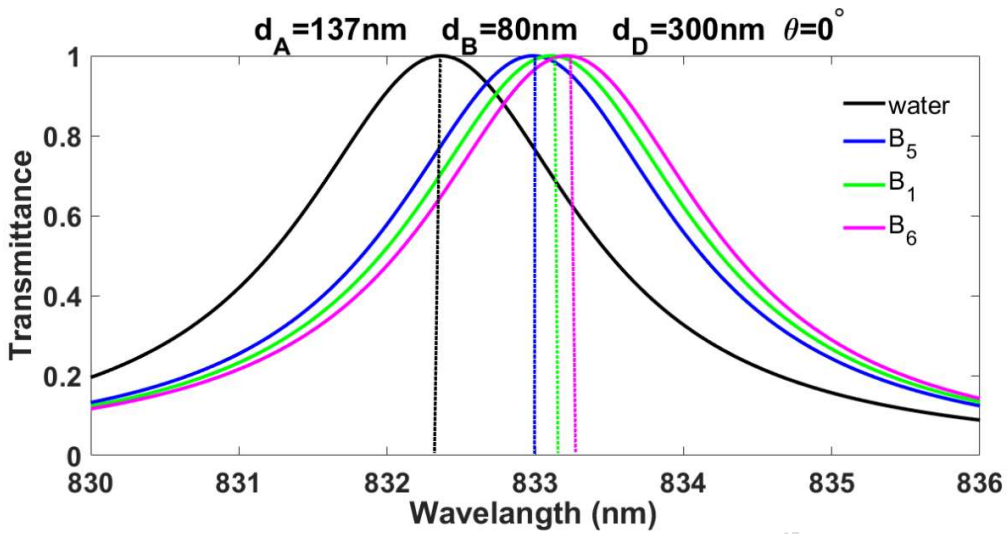

Fig. 1: Transmission spectra as a function of wavelength at normal incidence angle $\theta = 0^{\circ}$ for water and selected water soluble vitamins with concentration of 1g/50 mL.

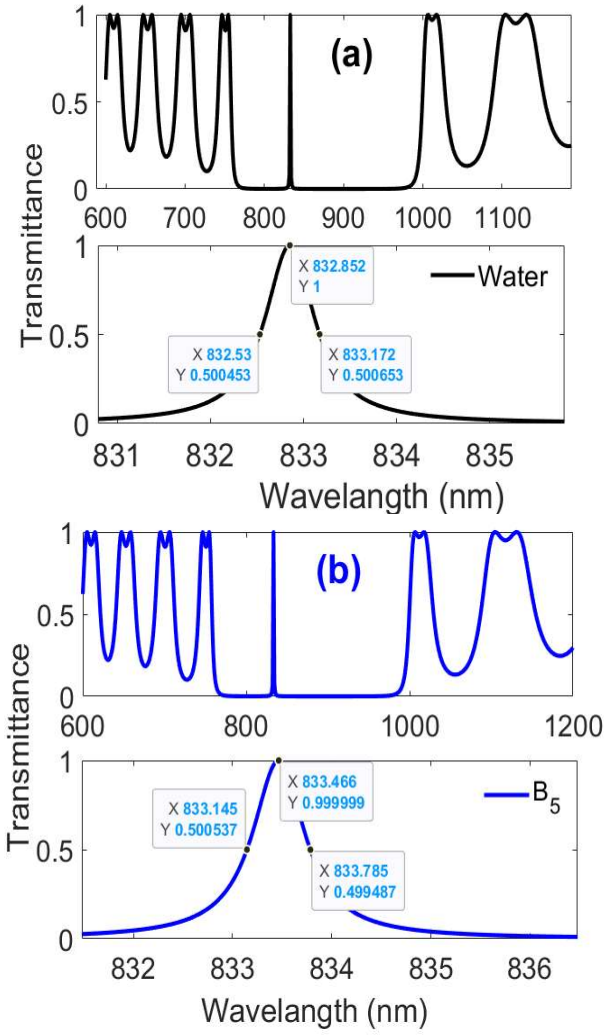

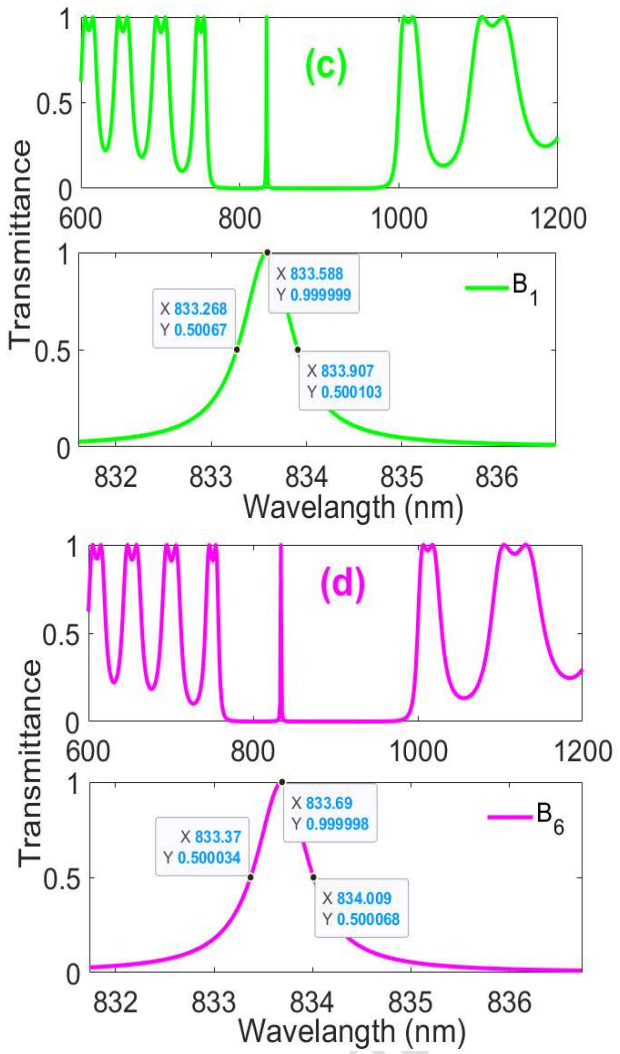

Fig. 2: Detailed performance analysis of each vitamin based on Fig. 1 at normal incidence angle $\theta = 0^{\circ}$.(a) water, (b) B_5, (c) B_1, (d) B_6.

Figure 1 presents the transmission spectra for the structure with defect filled with pure water (n=1.333) and aqueous solutions of the three vitamins (B_1, B_5, and B_6) at a concentration of 1g/50mL. The spectra are calculated at normal incidence. There is no distinction is observed between TE and TM polarizations. The spectrum for water reveals a well-defined PBG in the near-infrared region, with a sharp resonant peak located at approximately 830 nm. The introduction of vitamin solutions into the cavity induces a red-shift for B_5 (833.47 nm) (Fig. 2b), B_1 (833.59 nm) (Fig. 2c), and B_6 (833.69 nm) (Fig. 2d). This shift

is proportional to the refractive index of the analyte (see Table 2). The biosensor performance results summarized in Table 3, derived from the parameters in Table 2.

Table 2: Resonant Wavelength (λ_0), resonance shift ($\Delta\lambda_0$) and full width at half maximum ($\Delta\lambda_{FWHM}$) at normal incident angle ($\theta = 0^\circ$).

Defect	Refractive Index	Resonant Wavelength λ_0 (nm)	$\Delta n = n - n_0$	$\Delta\lambda_0 = [\lambda_0(n) - \lambda_0(n_0)]$ (nm)	$\Delta\lambda_{FWHM}$ (nm)
Water	$1.333 = n_{solvent}$	852.832	0	0	0.642
Vitamin B_5	~1.3360	833.466	0.003	0.614	0.640
Vitamin B_1	~1.3366	833.588	0.0036	0.736	0.639
Vitamin B_6	~1.3371	833.69	0.0041	0.838	0.639

Table 3: Quality Factor (Q), Sensitivity (S), Detection Limit (DL), and Figure of Merit (FOM) obtained from Table 2 at normal incident angle ($\theta = 0^\circ$).

Water Soluble Vitamin	Quality Factor ($Q = \lambda_0/\Delta\lambda_{FWHM}$)	Sensitivity ($S = \Delta\lambda_0/\Delta n$)	Detection Limit $(\lambda_0/SQ) \times 10^{-3}$	Figure of Merit ($S \cdot Q/\lambda_0$)
Vitamin B_5	1302.29	204.66	3.12	319.78
Vitamin B_1	1304.51	204.44	3.12	319.93
Vitamin B_6	1304.67	204.39	3.12	319.85

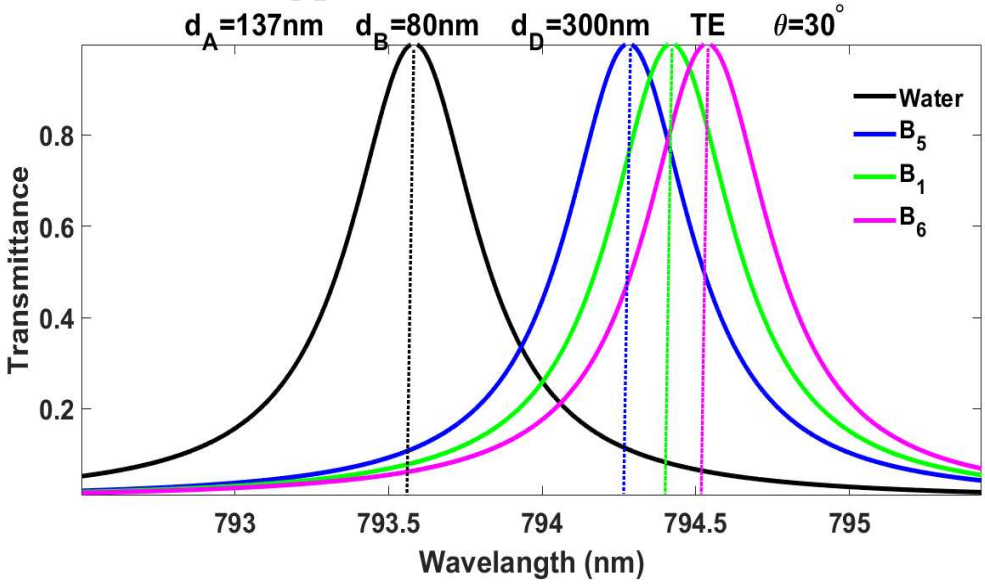

Fig. 3: Resonance modes at incident angle $\theta = 30^{\circ}$ and for TE polarization wave.

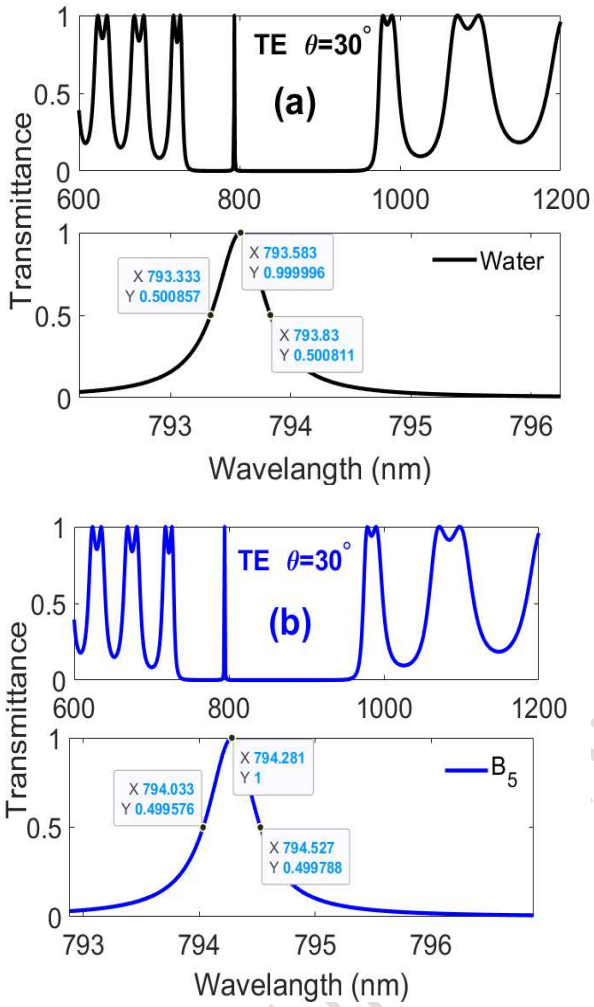

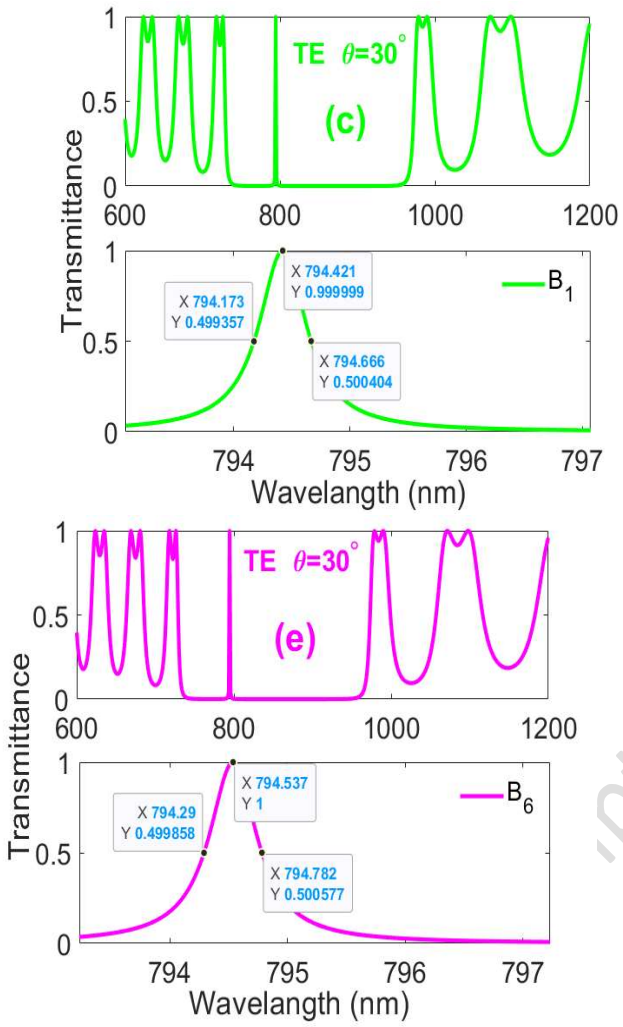

Fig. 4: Detailed resonance analysis of each water soluble vitamin based on Fig. 3 different at incident angle $\theta = 30^{\circ}$ *and for TE polarization wave*. (a) water, (b) B_5, (c) B_1, (d) B_6.

Figures 3 and 4 present the resonance behavior of the proposed photonic crystal at an incident angle of 30° for TE polarization. According to Fig. 4, the resonance wavelengths for water and vitamins B_5, B_1, and B_6 are about 793.58nm (Fig. 4a), 794.28nm (Fig. 4b), 794.42 nm (Fig. 4c), and 794.53 nm (Fig. 4d) repectively (see Table 4). As summarized in Table 4, the resonance wavelength shifts progressively from 793.58 nm for pure water (Fig. 4a) to 794.53 nm for vitamin B_6 (Fig. 4d). The device exhibits resonance

linewidths ($\Delta\lambda_{FWHM}$=0.49–0.50 nm), resulting high quality factors (Q=1600, Table 5). The sensitivity is above 230 nm/RIU, with detection limits near 2.1×10^{-3} RIU and FOM exceeding 470.

Table 4: *TE* Resonant Wavelength (λ_0), resonance shift ($\Delta\lambda_0$) and full width at half maximum ($\Delta\lambda_{FWHM}$) at incident angle $\theta = 30^\circ$.

Defect	Refractive Index	Resonant Wavelength λ_0 (nm)	$\Delta n=n-n_0$	$\Delta\lambda_0=[\lambda_0(n)-\lambda_0(n_0)]$ (nm)	$\Delta\lambda_{FWHM}$ (nm)
Water	1.333=$n_{solvent}$	793.583	0	0	0.497
Vitamin B_5	~1.3360	794.281	0.003	0.698	0.494
Vitamin B_1	~1.3366	794.421	0.0036	0.838	0.493
Vitamin B_6	~1.3371	794.537	0.0041	0.954	0.492

Table 5: *TE* Quality Factor (Q), Sensitivity (S), Detection Limit (DL), and Figure of Merit (FOM) obtained from Table 4 at incident angle $\theta = 30^\circ$.

Water Soluble Vitamin	Quality Factor ($Q=\lambda_0/\Delta\lambda_{FWHM}$)	Sensitivity ($S=\Delta\lambda_0/\Delta n$)	Detection Limit $(\lambda_0/SQ)\times10^{-3}$	Figure of Merit ($S\cdot Q/\lambda_0$)
Vitamin B_5	1607.856	232.666	2.123	470.983
Vitamin B_1	1611.401	232.777	2.117	472.164
Vitamin B_6	1614.912	232.682	2.114	472.93

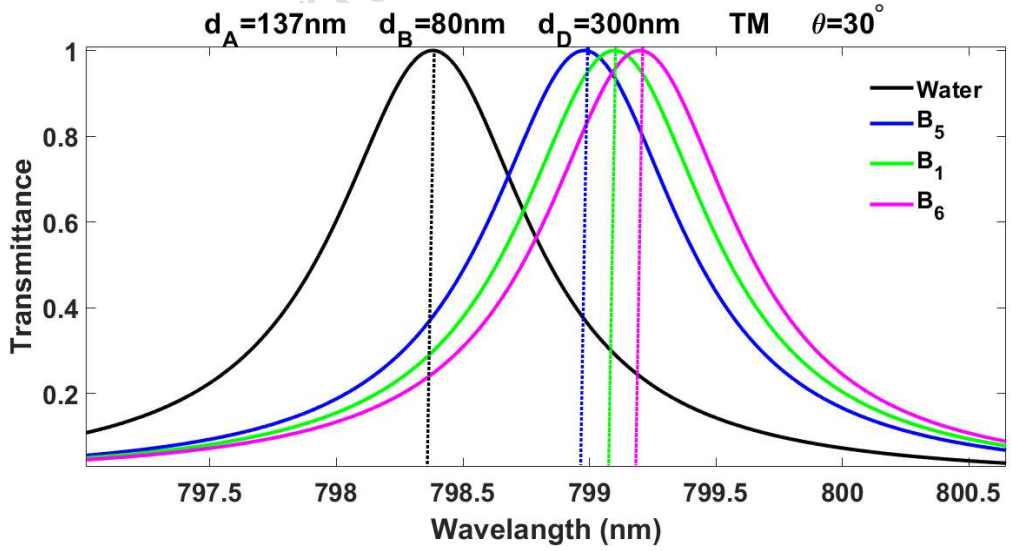

Fig. 5: Resonance modes at incident angle $\theta = 30^\circ$ and for TM polarization wave.

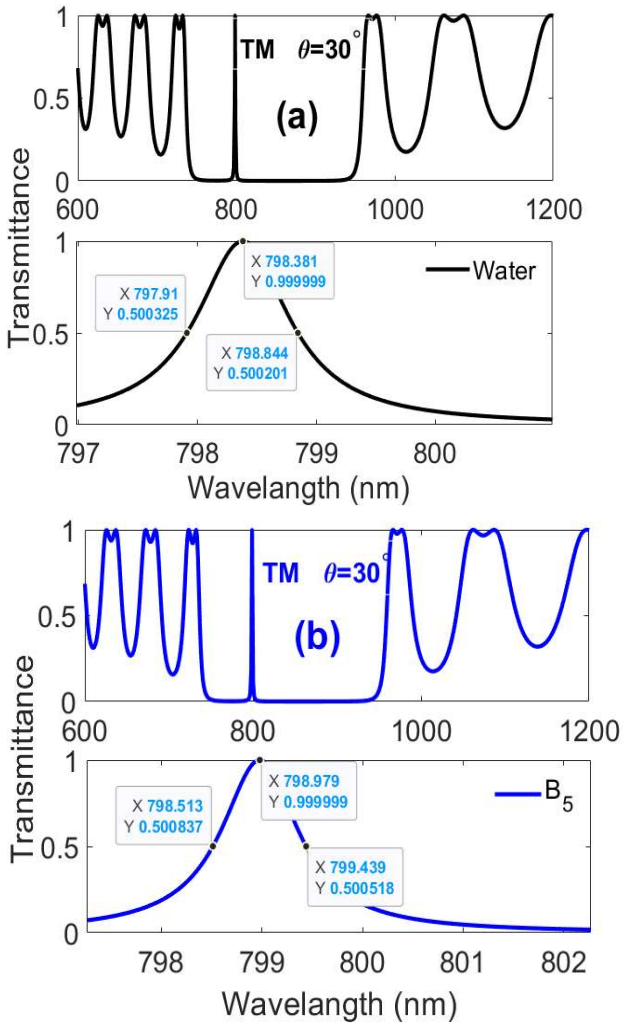

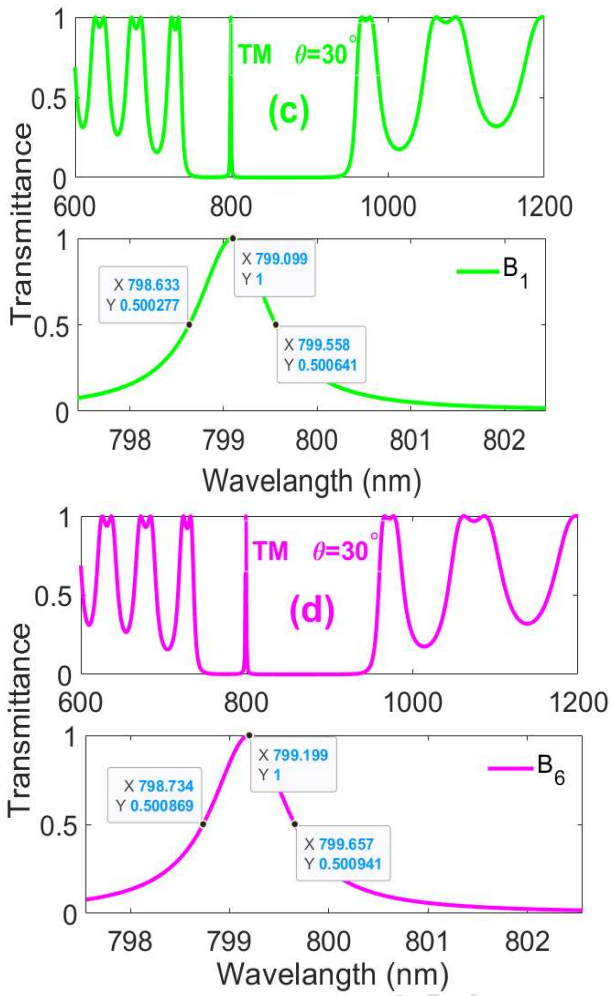

Fig. 6: Detailed resonance analysis of each water soluble vitamin based on Fig. 5 different at incident angle $\theta = 30^{\circ}$ *and for TM polarization wave*. (a) water, (b) B_5, (c) B_1, (d) B_6.

Figures 5 and 6 present the resonance spectra of the proposed photonic crystal resonator at an incident angle of 30° under TM polarization for water-soluble vitamin defect layers. Figure 5 illustrates the overall transmission response, while Figure 6 provides a detailed view of the resonance peaks for each vitamin. According to Fig. 6, the resonance wavelengths for water and vitamins B_5, B_1, and B_6 are about 798.38nm (Fig. 6a), 798.97nm (Fig. 6b), 799.1 (Fig. 6c), and 799.2 nm (Fig. 6d) repectively (see Table 6). Compared to the TE polarization at the same angle, the TM mode exhibits broader linewidths

and lower Q-factors (Q~860) and reduced FOM (~215), whereas TE mode reached Q>1600 and FOM> 470 (see Tables 5, 7).

Table 6: *TM* Resonant Wavelength (λ_0), resonance shift ($\Delta\lambda_0$) and full width at half maximum ($\Delta\lambda_{FWHM}$) at incident angle $\theta = 30^\circ$.

Defect	Refractive Index	Resonant Wavelength λ_0 (nm)	$\Delta n = n - n_0$	$\Delta\lambda_0 = [\lambda_0(n) - \lambda_0(n_0)]$ (nm)	$\Delta\lambda_{FWHM}$ (nm)
Water	$1.333 = n_{solvent}$	798.381	0	0	1.001
Vitamin B_5	~1.3360	798.979	0.003	0.598	0. 926
Vitamin B_1	~1.3366	799.099	0.0036	0.718	0.925
Vitamin B_6	~1.3371	799.199	0.0041	0.818	0.92

Table 7: *TM* Quality Factor (Q), Sensitivity (S), Detection Limit (DL), and Figure of Merit (FOM) obtained from Table 6 at incident angle $\theta = 30^\circ$.

Water Soluble Vitamin	Quality Factor ($Q = \lambda_0/\Delta\lambda_{FWHM}$)	Sensitivity ($S = \Delta\lambda_0/\Delta n$)	Detection Limit ($\lambda_0/SQ) \times 10^{-3}$	Figure of Merit ($S \cdot Q/\lambda_0$)
Vitamin B_5	862.828	199.333	4.645	215.262
Vitamin B_1	863.89	199.444	4.637	215.614
Vitamin B_6	860.694	199.512	4.654	214.863

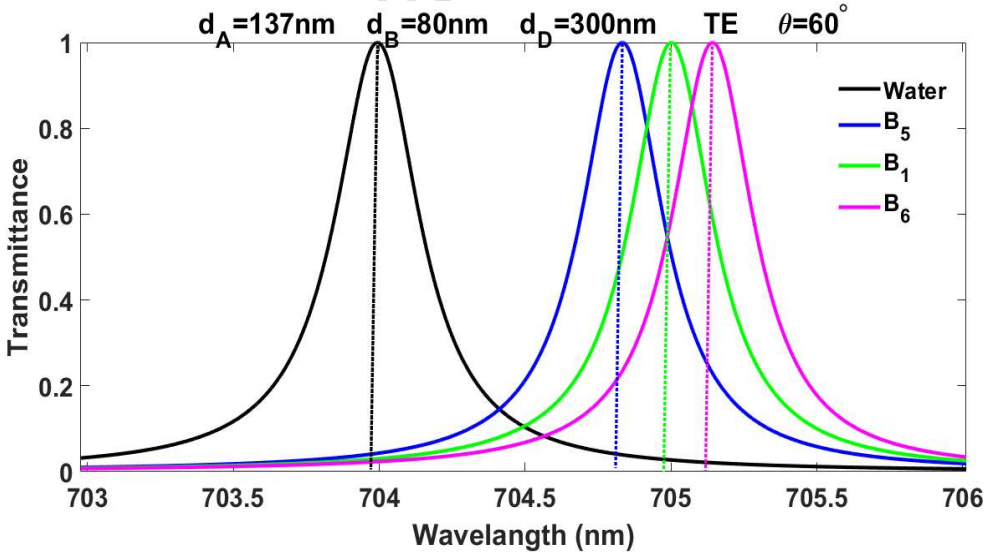

Fig. 7: Resonance modes at incident angle $\theta = 60^\circ$ and for TE polarization wave.

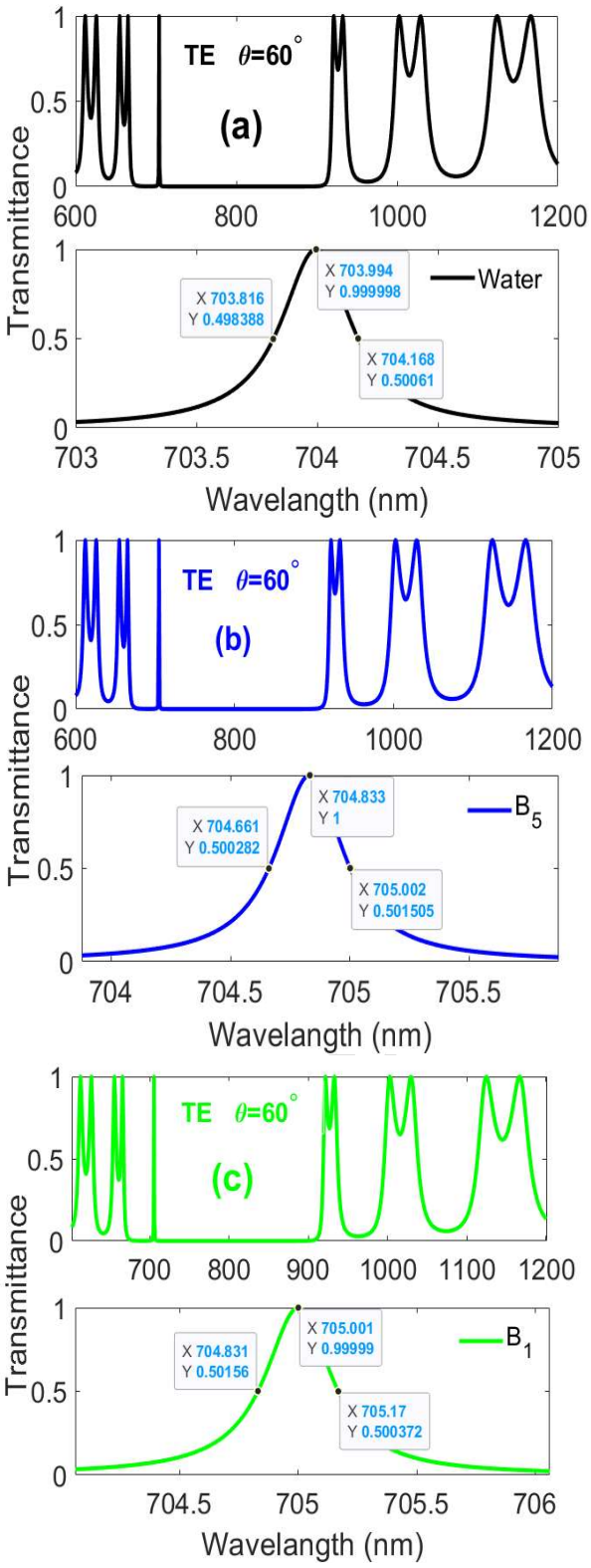

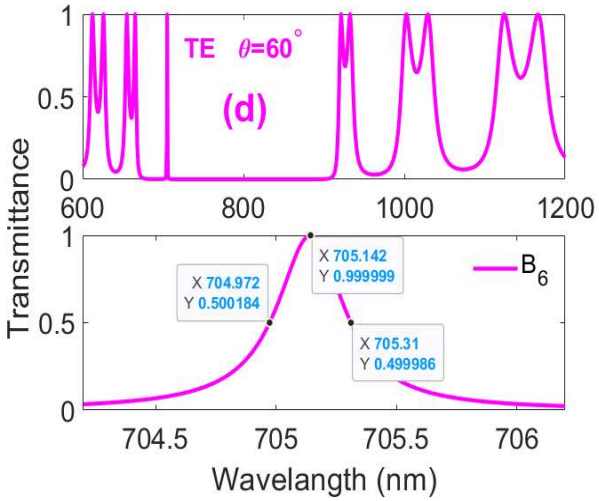

Fig. 8: Detailed resonance analysis of each water soluble vitamin based on Fig. 5 different at incident angle $\theta = 60^{\circ}$ *and for TE polarization wave*. (a) water, (b) B_5, (c) B_1, (d) B_6.

Figures 7 and 8 and corresponding performance analysis in Tables 8, 9 show the sensor's response at incidence angle of θ=60° for TE waves. The results demonstrate a significant improvement in nearly all performance metrics compared to θ=0°and θ=30°. According to Fig. 8, the resonance wavelengths for water and vitamins B_5, B_1, and B_6 are about 704nm (Fig. 8a), 704.83 nm (Fig. 8b), 705nm (Fig. 8c), and 705.14nm (Fig. 8d) repectively. The striking improvement is in the quality factor, which exceeds 2000 for all selected vitamins. This high Q-factor is a direct result of the narrowed resonance linewidth ($\Delta\lambda_{FWHM}$=0.34 nm). Consequently, the DL is significantly enhanced to 1.23×10^{-3} RIU, which is 2.5 times lower (i.e., better) than the DL at normal incidence (3.12×10^{-3} RIU). Furthermore, the sensitivity increases from 205 to 280 nm/RIU. Also, the FOM exceeds 800, which is more than 2.5 times greater than the FOM at normal incidence (320).

A sensitivity of 280 nm/RIU is high for refractometric sensors and, combined with the measured narrow linewidth (high Q), yields a low detection limit (1.2×10^{-3} RIU in our TE/60° case). In this case, for Δn=0.001, a sensitivity of 280 nm/RIU yields Δλ=0.28 nm. Our sensor's resonance linewidth in this configuration is less than 0.35 nm, this 0.28 nm shift is easily detectable and resolvable by a standard optical spectrometer. Therefore, this level of sensitivity is useful and meaningful for the quantitative

detection of target vitamins in the concentration range of interest. Thus S=280 nm/RIU is a suitable baseline for label-free refractometric detection for many vitamin concentrations.

Table 8: *TE* Resonant Wavelength (λ_0), resonance shift ($\Delta\lambda_0$) and full width at half maximum ($\Delta\lambda_{FWHM}$) at incident angle $\theta = 60^\circ$.

Defect	Refractive Index	Resonant Wavelength λ_0 (nm)	$\Delta n = n - n_0$	$\Delta\lambda_0 = [\lambda_0(n) - \lambda_0(n_0)]$ (nm)	$\Delta\lambda_{FWHM}$ (nm)
Water	1.333=$n_{solvent}$	703.994	0	0	0.352
Vitamin B_5	~1.3360	704.833	0.003	0.839	0. 344
Vitamin B_1	~1.3366	705.001	0.0036	1.007	0.339
Vitamin B_6	~1.3371	705.142	0.0041	1.148	0.338

Table 9: *TE* Quality Factor (Q), Sensitivity (S), Detection Limit (DL), and Figure of Merit (FOM) obtained from Table 8 at incident angle $\theta = 60^\circ$.

Water Soluble Vitamin	Quality Factor ($Q=\lambda_0/\Delta\lambda_{FWHM}$)	Sensitivity ($S=\Delta\lambda_0/\Delta n$)	Detection Limit ($\lambda_0/SQ)\times 10^{-3}$	Figure of Merit ($S\cdot Q/\lambda_0$)
Vitamin B_5	2048.933	279.666	1.23	812.982
Vitamin B_1	2079.648	279.722	1.211	825.138
Vitamin B_6	2086.218	280	1.207	828.401

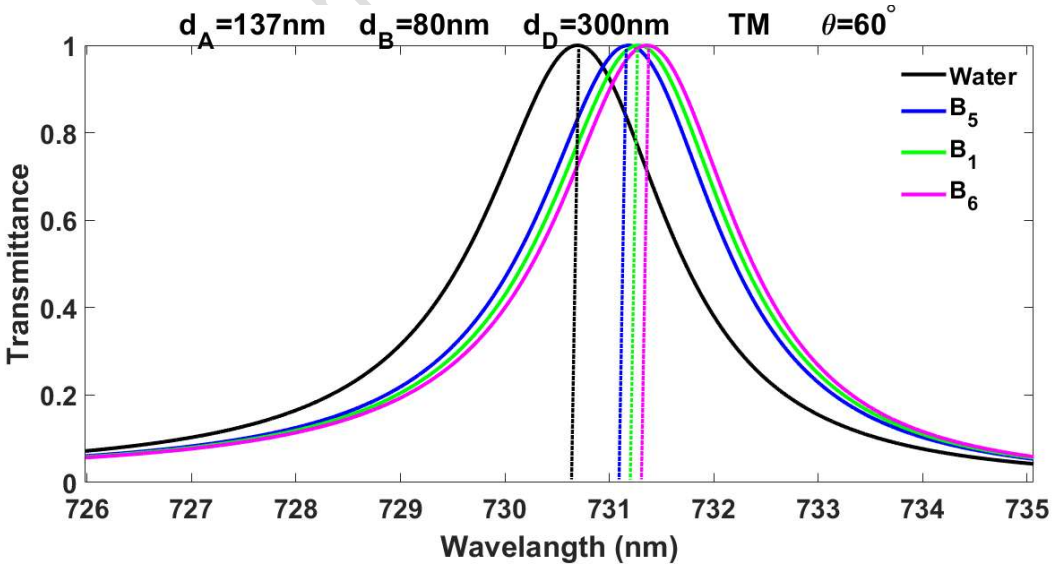

Fig. 9: Resonance modes at incident angle $\theta = 60^\circ$ and for TM polarization wave.

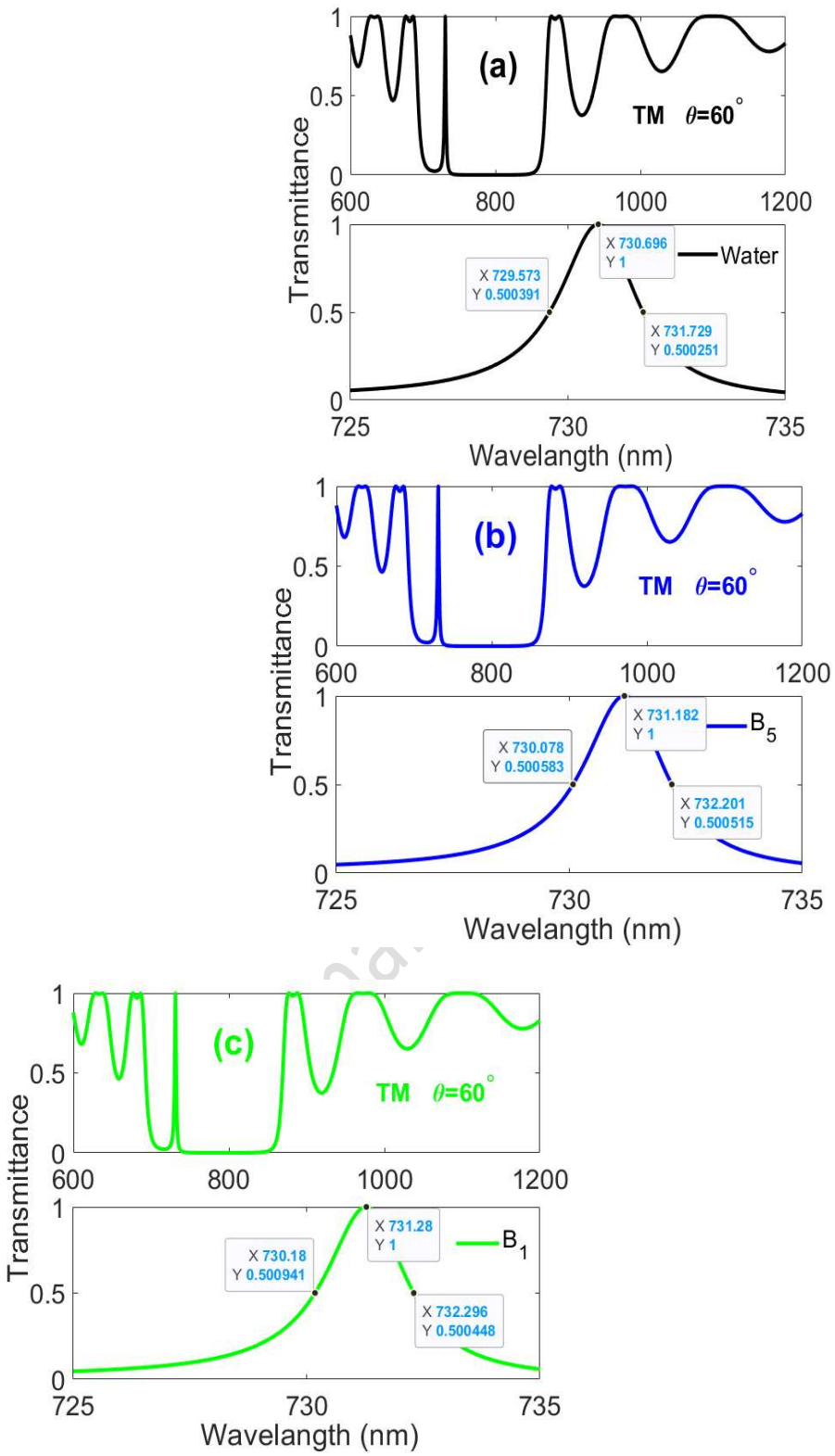

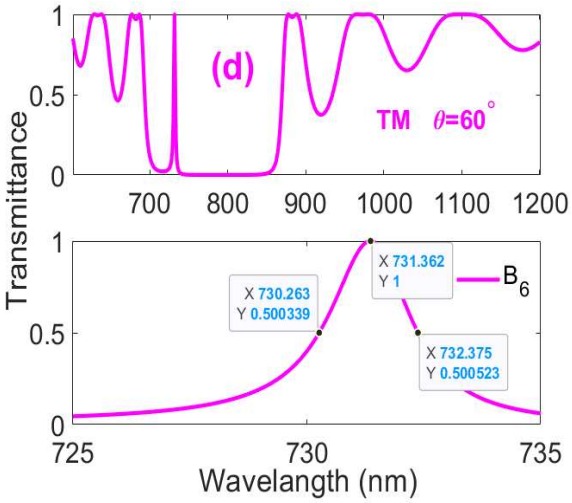

Fig. 10: Detailed resonance analysis of each water soluble vitamin based on Fig. 5 different at incident angle $\theta = 60^{\circ}$ *and for TM polarization wave*. (a)water, (b) B_5, (c) B_1, (d) B_6.

Figure 9 presents the transmission spectra for TM waves at an incident angle of 60°, while Figure 10 provides a detailed analysis of the sensor performance. The results demonstrate a significant degradation in performance compared to those in the TE polarization (see Tables 10, 11). According to Fig. 10, the resonance wavelengths for water and vitamins B_5, B_1, and B_6 are about 730.96nm (Fig. 10a), 731.18nm (Fig. 10b), 731.28nm (Fig. 10c), and 731.36nm (Fig. 10d) repectively. The resonant peaks for TM polarization are broad, with a $\Delta\lambda_{FWHM}$ exceeding 2.1 nm, which is more than 6 times wider than the peaks for TE polarization at 60° (0.34 nm). This result leads to low quality factor of only 345, which is nearly 6 times lower than the Q-factor for TE polarization at the same angle (2080). Furthermore, the sensitivity and FOM are reduced to a very low value compared to the TE polarization. The reason for the significant reduction in performance is Brewster angle. At the SiO_2/TiO_2 interfaces used in our stack, the Brewster angle condition occurs near the oblique angle (θ_B=59.7°). For TM polarization the Fresnel reflection coefficient goes to zero at this angle, so TM reflectivity collapses near θ_B and the photonic bandgap weakens, and the cavity defect cannot form a narrow high-Q resonance. But, TE polarization does not have a zero-reflection condition at that angle, so TE retains reflectivity.

Table 10: *TM* Resonant Wavelength (λ_0), resonance shift ($\Delta\lambda_0$) and full width at half maximum ($\Delta\lambda_{FWHM}$) at normal incident angle ($\theta = 60^\circ$)

Defect	Refractive Index	Resonant Wavelength λ_0 (nm)	$\Delta n = n - n_0$	$\Delta\lambda_0 = [\lambda_0(n) - \lambda_0(n_0)]$ (nm)	$\Delta\lambda_{FWHM}$ (nm)
Water	$1.333 = n_{solvent}$	730.969	0	0	2.156
Vitamin B_5	~1.3360	731.182	0.003	0.213	2.123
Vitamin B_1	~1.3366	731.28	0.0036	0.311	2.116
Vitamin B_6	~1.3371	731.362	0.0041	0.392	2.112

Table 11: *TM* Quality Factor (Q), Sensitivity (S), Detection Limit (DL), and Figure of Merit (FOM) obtained from Table 8 at incident angle $\theta = 60^\circ$.

Water Soluble Vitamin	Quality Factor ($Q = \lambda_0/\Delta\lambda_{FWHM}$)	Sensitivity ($S = \Delta\lambda_0/\Delta n$)	Detection Limit ($\lambda_0/SQ) \times 10^{-3}$	Figure of Merit ($S \cdot Q/\lambda_0$)
Vitamin B_5	344.409	71	29.901	33.443
Vitamin B_1	345.595	86.388	24.494	40.826
Vitamin B_6	346.288	95.853	22.033	45.384

Finally, Table 12 provides a final summary of the biosensor's key results from the study. It shows a comparison of how the sensor's performance is affected by changing the incident angle and polarization.

Table 12: Summary table (performance comparison).

Angle	Polarization	Sensitivity	Q-Factor	FOM	DL [$\times 10^{-3}$]
0°	TE/TM	204.7	1303	320	3.12
30°	TE	232.7	1610	472	2.12
30°	TM	199.5	862	215	4.64
60°	TE	280	2080	825	1.21
60°	TM	43 - 96	345	20 - 45	22 - 49

About optimum angle 60°, we can say that at this angle the effective optical path inside each layer increases. This result causes a large phase shift per layer, which directly strengthens the Bragg condition, expressed as $2(n_A d_A \cos\theta_{tA}+n_B d_B \cos\theta_{tB})=m\lambda$. When $\cos\theta_t$ becomes small at 60°, the terms $n.d.\cos\theta_t$ grows, yielding stronger constructive interference and higher reflectivity (higher Q). Because sensitivity is proportional to $\Delta\lambda/\Delta n$, a higher Q produces a pronounced wavelength shift. Therefore, the increased optical path and strengthened Bragg reflection at 60° directly enhance the biosensor performance.

4. Conclusions

We designed an optical sensor that can detect three water-soluble vitamins without using any labels and only by measuring small changes in refractive index. Our simulations showed that both the angle of the incident and polarization strongly affect the sensor's performance. The best results were obtained when the light entered the structure at a 60° angle with TE polarization, where the sensor achieved high sensitivity (about 280 nm/RIU), a very sharp resonance peak (Q greater than 2000), and a low detection limit (about 1.21×10^{-3}). In contrast, using TM polarization at high angles reduced the sensor's effectiveness because of Brewster's angle, which decreases reflected light for TM waves. Overall, these findings give a clear guideline for designing this type of sensor and show that the proposed structure can detect multiple vitamins at the same time. To become a practical device, this sensor must solve several real-world challenges. Its performance depends on extremely precise manufacturing to avoid tiny errors that degrade the signal. The design is sensitive to specific angles and light polarization, which are hard to maintain. Temperature changes and unwanted substances in samples can affect the results.

Data availability: Data will be made available on request.

Funding: Not Applicable.

Competing Interest: Not Applicable.

References:

[1] Lu, H., Li, W., Xue, C.-H., Jiang, H., Jiang, X., & Chen, H. (2013). High-efficiency nonlinear platform with usage of metallic nonlinear susceptibility. Optics Letters, *38*, 1283–1285. https://doi.org/10.1364/OL.38.001283

[2] Lu, H., Li, Y., Feng, T., Wang, S., Xue, C., Kang, X., Du, G., Jiang, H., & Chen, H. (2013). Optical Tamm states in hetero-structures with highly dispersive planar plasmonic metamaterials. Applied Physics Letters, 102(11). https://doi.org/10.1063/1.4795532

[3] Lu, H., Wang, Q., Yang, D., Sun, J., Liu, H.-C., Shen, K.-S., Dong, C., Zhu, Z.-L., & Dong, S.-Q. (2025). Reverse design of metasurface enhanced human infrared absorption based on the extinction properties. Optics Letters, *50*, 5654–5657. https://doi.org/10.1364/OL.566616

[4] Dong, S., Yang, D., Wang, Q., Hu, H., Sun, J., Shen, K., Dong, C., Liu, H., Zhu, Z., & Lu, H. (2025). Modularized control of broadband surface-enhanced infrared absorption spectroscopy realized in over-coupled metasurfaces. Chinese Optics Letters, *23*(5), 053602. https://doi.org/10.3788/COL202523.053602

[5] Dong, S., Dong, C., Shen, K., Zheng, Y., Sun, J., Zhen, C., Hu, H., Zhang, F., Zhang, Z., Liu, H., & Lu, H. (2023). Wavelength multiplexing infrared metasurfaces for protein recognition and trace detection. Nanophotonics, 12(20), 3963–3976. https://doi.org/10.1515/nanoph-2023-0517

[6] Ramola, A., Shakya, A. K., Droby, A., & Bergman, A. (2025). Numerical study of a novel kagome-inspired photonic crystal fiber-based surface plasmon resonance biosensor for detection of blood components and analytical targets. Biosensors, 15(8), 539. https://doi.org/10.3390/bios15080539

[7] Ramola, A., Shakya, A. K., Kumar, V., & Bergman, A. (2025). Recent advances in photonic crystal fiber-based SPR biosensors: Design strategies, plasmonic materials, and applications. Micromachines, 16(7), 747. https://doi.org/10.3390/mi16070747

[8] Ramola, A., Shakya, A. K., & Bergman, A. (2025). Finite element method-based modeling of a novel square photonic crystal fiber surface plasmon resonance sensor with a Au–TiO_2 interface and the relevance of artificial intelligence techniques in sensor optimization. Photonics, 12(6), 565. https://doi.org/10.3390/photonics12060565

[9] Shakya, A. K., & Singh, S. (2023). Development of a generalized Fourier transform model for distinct household oil samples by performing spectroscopy analysis. Results in Optics, 10, 100355. https://doi.org/10.1016/j.rio.2023.100355

[10] Ramola, A., Shakya, A. K., Vidyarthi, A., Singh, S., Talker, E., & Bergman, A. (2025). Next-generation photonic-crystal-fiber-based plasmonic sensor for heavy metal detection via spectroscopy and refractive index integration. Proceedings of SPIE, 13639, 13639AJ. https://doi.org/10.1117/12.3062891

[11] Ramola, A., Marwaha, A., & Singh, S. (2023). Design of a triple-layered plasmonic biosensor for glucose monitoring from urine sample for diabetes prevention. MAPAN, 38, 511–525. https://doi.org/10.1007/s12647-022-00610-0

[12] Ramola, A., Marwaha, A., & Singh, S. (2024). Pregnancy detection through modelling of dual-polarized plasmonic PREGBIOSENSOR by urine samples analysis. Plasmonics, 19, 33–49. https://doi.org/10.1007/s11468-023-01962-2

[13] Shangbo, Y., Jin, Z., & Jing, Y. (2023). Analysis of the water-soluble vitamins based on MIM waveguide structure and Fano resonance. Heliyon, 9, e15234. https://doi.org/10.1016/j.heliyon.2023.e15094

[14] Sun, Y., Ren, Y., Qu, D., Qin, F., & Li, C. (2024). Plasmonic sensor based on S-shaped metal-insulator-metal waveguide for the detection of water-soluble vitamins. Plasmonics. https://doi.org/10.1007/s11468-024-02506-y

[15] Wang, N., Liu, B., Wu, X., & Peng, Y. (2024). Novel THz metasurface biosensor for high-sensitivity detection of vitamin C and vitamin B9. Photonics, 11, 820. https://doi.org/10.3390/photonics11090820

[16] Banan Khojasteh, M. H., Sohrabi, H., & Majidi, M. R. (2025). A critical review of electrochemical and optical vitamin B6 sensing: Evolution of biosensor platforms based on advanced nanosystems. Critical Reviews in Food Science and Nutrition, 65, 4243–4263. https://doi.org/10.1080/10408398.2024.2386037

[17] Draz, M. U., Yaqub, A., Jafry, A. T., Khan, M., & Ajab, H. (2024). Electrochemical sensing of B-complex vitamins: Current challenges and future prospects with microfluidic integration. RSC Advances, 14, 10331–10347. https://doi.org/10.1039/D4RA00555D

[18] Sohrabnezhad, S., Pourahmad, A., Sadjadi, M. S., & Sadeghi, B. (2008). Nickel cobalt sulfide nanoparticles grown on AlMCM-41 molecular sieve. Physica E, 40(3), 684–688. https://doi.org/10.1016/j.physe.2007.09.081

[19] Sadeghi, B., & Vahdati, R. A. R. (2012). Comparison and SEM-characterization of novel solvents of DNA/carbon nanotube. Applied Surface Science, 258(7), 3086–3088. https://doi.org/10.1016/j.apsusc.2011.11.042

[20] Azari, B., Pourahmad, A., Sadeghi, B., & Mokhtary, M. (2023). Green synthesis of SiO_2 from Equisetum arvense plant for synthesis of SiO_2/ZIF-8 MOF nanocomposite as photocatalyst. Journal of Coordination Chemistry, 76(2), 219–231. https://doi.org/10.1080/00958972.2023.2166408

[21] Pourjafari, M., Ghane, M., Kaboosi, H., Sadeghi, B., & Rezaei, A. (2022). Antibacterial properties of Ag–Cu alloy nanoparticles against multidrug-resistant Pseudomonas aeruginosa through inhibition of quorum sensing pathway and virulence-related genes. Journal of Biomedical Nanotechnology, 18(4), 1196–1204. https://doi.org/10.1166/jbn.2022.3331

[22] Khodadad, H., Hatamjafari, F., Pourshamsian, K., Sadeghi, B. (2021). Microwave-assisted synthesis of novel pyrazole derivatives and their biological evaluation as anti-bacterial agents. Combinatorial Chemistry & High Throughput Screening, 24(5), 695–700. https://doi.org/10.2174/1386207323666201019152206

[23] Zaky, Z. A., Alzahrani, A., Abu Radia, M. A., Zhaketov, V. D., El-Tokhy, M. S., & Sallah, M. (2025). Refractive indices equations of silicon dioxide for optical simulations. Journal of Optics, 1–32. https://doi.org/10.1007/s12596-025-02719-2

[24] Devore, J. R. (1951). Refractive indices of rutile and sphalerite. Journal of the Optical Society of America, 41, 416–419. https://doi.org/10.1364/JOSA.41.000416

[25] Gowdhami, D., Balaji, V. R., Murugan, M., Robinson, S., & Hegde, G. (2022). Photonic crystal-based biosensors: An overview. ISSS Journal of Micro and Smart Systems, 11, 147–167. https://doi.org/10.1007/s41683-022-00092-x

[26] Missoni, L. L., Ortiz, G. P., Ricci, M. L. M., Toranzos, V. J., & Mochán, W. L. (2020). Rough 1D photonic crystals: A transfer matrix approach. Optical Materials, 109, 110012. https://doi.org/10.1016/j.optmat.2020.110012